

# Accelerating target analyte measurement in resistive sensors: A multiplierless first-order differentiation method with SnS<sub>2</sub> gas sensor

Naveen Kumar Bandari, Srinivasulu Kanaparthi, Shiv Govind Singh <sup>\*</sup>

*Department of Electrical Engineering, Indian Institute of Technology Hyderabad, Kandi, Telangana 502284, India*



## ARTICLE INFO

**Keywords:**  
 Resistive sensor  
 Gas sensing  
 NH<sub>3</sub> gas sensor  
 SnS<sub>2</sub> nanostructures  
 First order differentiation  
 Transient analysis

## ABSTRACT

In various chemical sensing applications, rapid measurement of analyte concentrations is essential. While estimating the equilibrium response from initial transient responses provides a practical and cost-effective solution, existing techniques often involve extensive data, complex algorithms, or inefficiencies. This study presents a discrete multiplierless first-order differentiation method designed to expedite the measurement of NH<sub>3</sub> gas concentration using a resistive gas sensor composed of SnS<sub>2</sub> nanostructures at room temperature ( $25 \pm 3^\circ\text{C}$ ). This method significantly reduces stabilized response measurement time by transforming the sensor's monotonically changing response into a non-monotonic one and associating the resulting peaks with NH<sub>3</sub> gas concentration. Specifically, it makes gas concentration determination 85–94 % faster for concentrations ranging from 42 to 105 ppm than traditional steady-state measurements. This enhanced speed makes the method well-suited for resource-limited applications requiring rapid analyte quantification.

## 1. Introduction

Chemical sensors play a vital role in converting chemical information into electrical signals, making them indispensable in various fields such as environmental surveillance, medical care, risk management, and food safety inspection [1–4]. The ongoing advancements in this area have focused on enhancing sensor attributes like response, selectivity, detection limits, and energy efficiency. These improvements are largely driven by innovations in material production, device manufacturing, and characterization techniques [5–8]. A diverse range of gas sensors are available, including optical, electrochemical, quartz crystal microbalance (QCM), and resistive types [9–12]. Optical sensors provide high sensitivity but are expensive. Electrochemical sensors may suffer from electrode poisoning, affecting longevity and stability. QCM sensors are complex, require precise frequency measurements, and consume more power. Resistive gas sensors, however, offer simple fabrication, low cost, minimal complexity, and the ability to detect low gas concentrations, making them a promising choice for various applications. Despite the advantages offered by resistive sensors, they often suffer from slow response times, which can limit their effectiveness in real-time applications where timely and accurate results are critical. This need for rapid detection becomes particularly evident in scenarios such as hazardous gas monitoring, where detecting gases like NH<sub>3</sub> quickly is essential to

prevent accidents and minimize harm. The Occupational Safety and Health Administration (OSHA) sets a permissible exposure limit (PEL) of 50 ppm for NH<sub>3</sub> gas over a one-hour time-weighted average [13]. Similarly, in food quality monitoring, early detection of spoilage is crucial. NH<sub>3</sub> gas concentrations of 40–50 ppm often indicate the initial stages of meat decomposition [14–17]. Fast sensor responses enable quick assessments of food freshness and shelf life, benefiting both consumers and manufacturers. Moreover, rapid sensor response allows for accurate humidity calibration using known relative humidity (RH) versus response relationships. Slow response times, however, can render such calibrations ineffective, as dynamically changing ambient humidity during the sensor's response period may invalidate the calibration model [18,19].

While considerable research has focused on reducing measurement times through materials-based approaches, these methods often involve complex and costly processes, such as the intricate synthesis of advanced materials or the fabrication of sophisticated device structures [20,21]. These complexities can make implementation challenging and limit the widespread adoption of such techniques. Alternatively, signal analysis methods offer a more accessible and cost-effective alternative for accelerating measurement. These techniques are highly adaptable, as they do not depend on the specific materials or device architectures used in the sensor. Furthermore, they can be seamlessly integrated with other

\* Corresponding author.

E-mail address: [sgsingh@ee.iith.ac.in](mailto:sgsingh@ee.iith.ac.in) (S.G. Singh).

methods to improve the efficiency of the sensing platform. A few signal processing strategies have been recommended to shorten sensor measurement time. These include transient response analysis using curve fitting, the pairing number method, the exponential moving average, and the application of neural networks [22–31]. Curve fitting is one common approach, but it reduces measurement time by only  $\sim 45\%$ . While neural networks can be effective, they typically require substantial computational resources and large datasets for training, which can be a significant drawback in many applications. The pairing number method, although simpler, may not be efficient due to its response to small variations in the temporal response of the sensor. This response can result in large fluctuations in the pairing number, leading to inaccuracies in the measurement. Although the exponential moving average filter and time-normalized response methods effectively reduce measurement time, they still require a multiplier or divider, which consumes a significant portion of resources and limits their applicability in resource-constrained environments.

To address the challenges of rapid sensor measurements with minimal computational requirements, this study introduces a novel technique that employs first-order differentiation in the discrete domain to minimize analysis time. The method was validated using an  $\text{SnS}_2$  resistive sensor exposed to  $\text{NH}_3$  gas concentrations ranging from 10.2 to 105 ppm at ambient temperature ( $25 \pm 3^\circ\text{C}$ ). Conducting polymers, metal oxides, and two-dimensional (2D) materials are commonly employed for gas detection applications [32–34]. Additionally, materials such as metal chalcogenides and van der Waals materials can be utilized for gas sensing due to their exceptional optical properties, which can significantly enhance sensing performance [35–39]. Specifically, for  $\text{NH}_3$  gas detection, conducting polymers, including polyaniline (PANI), polypyrrole (PPy), and polythiophene (PTh), are extensively used in resistive gas sensors owing to their tunable conductivity and ease of synthesis. However, their performance tends to degrade over time due to environmental instability [40]. While highly effective, metal oxides often require high operating temperatures for optimal performance, increasing power consumption [33]. Among 2D materials, metal sulfides have emerged as promising candidates for gas sensing applications.  $\text{SnS}_2$ , in particular, was chosen for this work due to its unique properties that make it well-suited for gas sensing. It offers excellent chemical stability, a high surface area, and outstanding semiconducting properties that enhance sensitivity to gas molecules [41]. Its layered structure and high density of active sites enable efficient adsorption and desorption of  $\text{NH}_3$  gas, ensuring a strong and reversible sensing response. The sensor's response was transformed from a monotonically increasing exponential curve to a nonmonotonic reaction, with peak values mapped to  $\text{NH}_3$  gas concentration through a power-law correlation. The response for concentrations below 40 ppm was low, necessitating the use of this method for concentrations above 40 ppm. This technique led to an 85–94 % reduction in maximum response measurement time for  $\text{NH}_3$  gas concentrations above 40 ppm. Moreover, it is computationally efficient, avoiding complex data processing algorithms, making it a practical and scalable solution for real-time gas sensing applications.

## 2. Experimental section

### 2.1. Materials

Tin (IV) Chloride Pentahydrate ( $\text{SnCl}_4 \cdot 5 \text{ H}_2\text{O}$ , 98 %) was procured from Sigma-Aldrich, USA; Thioacetamide ( $\text{C}_2\text{H}_5\text{NS}$ , 99 %) was sourced from Sisco Research Laboratories Pvt. Ltd, India; and Ethanol ( $\text{C}_2\text{H}_5\text{OH}$ , 99.9 %) was acquired from Changshu Hongsheng Fine Chemicals, China.

### 2.2. Synthesis of $\text{SnS}_2$ nanostructures

The synthesis of  $\text{SnS}_2$  nanostructures follows the solvothermal method, as shown in Fig. S1. in the [Supplementary Information](#). It

begins with dissolving 0.35 g of  $\text{SnCl}_4 \cdot 5 \text{ H}_2\text{O}$  and 0.40 g of  $\text{C}_2\text{H}_5\text{NS}$  in 40 mL of alcohol. This solution is then placed into a 100 mL autoclave and subjected to 15 hours of heating at  $160^\circ\text{C}$  in an oven, which naturally cools to room temperature. The resulting product undergoes several washes with ethanol and deionized water using centrifugation to eradicate impurities and is dried overnight in an oven at  $60^\circ\text{C}$ , yielding well-defined  $\text{SnS}_2$  nanostructures.

### 2.3. Material characterization

The  $\text{SnS}_2$  nanostructure's crystal structure is performed through Powdered X-ray Diffraction (PXRD) within a  $2\theta$  range spanning from  $20^\circ$  to  $60^\circ$ . This examination is conducted at  $0.02^\circ$  scan rate per second, utilizing  $\text{Cu K}\alpha 1$  radiation ( $\lambda=1.5402 \text{ \AA}$ ). Furthermore, the  $\text{SnS}_2$  nanostructure's surface morphology was conducted through Field-emission Scanning Electron Microscopy (FESEM) with a JEOL JSM 7800 F instrument. During the FESEM analysis, a working distance and accelerating voltage of 9.9 mm and 10 kV were employed to attain high-resolution photographs that provide detailed insights into the nanostructure's surface characteristics. A PHI 5000 VERSA PROBE III instrument was utilized to analyze X-ray photoelectron Spectroscopy (XPS). The XPS setup featured a non-monochromated  $\text{Al K}\alpha$  X-ray source with 1486.6 eV of photon energy ( $h\nu$ ), coupled with a double-focusing total  $180^\circ$  hemispherical analyzer for characterizing the  $\text{SnS}_2$  nanostructures. To ensure accuracy, the binding energies of all peaks observed for the  $\text{SnS}_2$  nanostructures were calibrated against the adventitious carbon C 1 s peak, which typically appears at a binding energy of 284.8 eV.

### 2.4. Device fabrication and sensing

Gas sensor measurements were performed using a custom-designed gas-sensing setup, as illustrated in Fig. S2. in the [Supplementary Information](#). To prepare the sensing material, 20 mg of  $\text{SnS}_2$  nanostructures were dissolved in 0.5 mL of ethanol and sonicated for 1 hour to ensure homogeneous dispersion of the nanoparticles. To fabricate the resistive sensor, 5  $\mu\text{L}$  of the prepared  $\text{SnS}_2$  nanostructure suspension was deposited onto a glass substrate with gold-patterned interdigitated electrodes (IDE) using a pipette, as shown in Fig. S3. in the [Supplementary Information](#). The IDE had the following dimensions: width of the finger ( $W_f$ ) =  $30 \mu\text{m}$ , spacing between the fingers ( $S_f$ ) =  $300 \mu\text{m}$ , and total number of fingers ( $N_f$ ) = 63. Once fabricated, the  $\text{SnS}_2$  resistive sensor was placed inside a sealed gas chamber to provide a controlled environment for sensing experiments. The sensor was connected to a Keithley 2450 Source Meter, which monitored and recorded the transient current response under a 5 V applied voltage. Experiments were conducted in various gaseous environments at room temperature, with relative humidity (RH) maintained at  $25 \pm 3^\circ\text{C}$  and  $25 \pm 5\%$ , respectively. For this study, all gas cylinders were balanced with synthetic air, composed of 79 % nitrogen ( $\text{N}_2$ ) and 21 % oxygen ( $\text{O}_2$ ), and procured from PHOENIX GASES PVT LTD, Mumbai, India. The certified concentration of  $\text{NH}_3$  gas was 105 ppm. To precisely control the  $\text{NH}_3$  gas concentration in the chamber, mass flow controllers (MFCs) were used to dilute the flow rates of synthetic air and  $\text{NH}_3$  gas. The MFCs maintained a constant total flow rate of 100 standard cubic centimeters per minute (sccm) into the chamber, enabling accurate control of  $\text{NH}_3$  gas concentrations. The  $\text{NH}_3$  gas concentrations were determined using equation S1, provided in the [Supplementary Information](#).

The gas chamber is first purged with synthetic air to allow the sensor to stabilize and reach a baseline current. Once the sensor's current has stabilized in synthetic air, a specific concentration of  $\text{NH}_3$  gas is introduced into the chamber by mixing synthetic air with  $\text{NH}_3$  gas. After the sensor's response to the  $\text{NH}_3$  gas reaches a steady state, the  $\text{NH}_3$  gas is replaced with synthetic air. Exposing the sensor to  $\text{NH}_3$  gas and allowing it to recover with synthetic air is repeated multiple times with different concentrations of  $\text{NH}_3$  gas. Each cycle provides data on how the sensor's

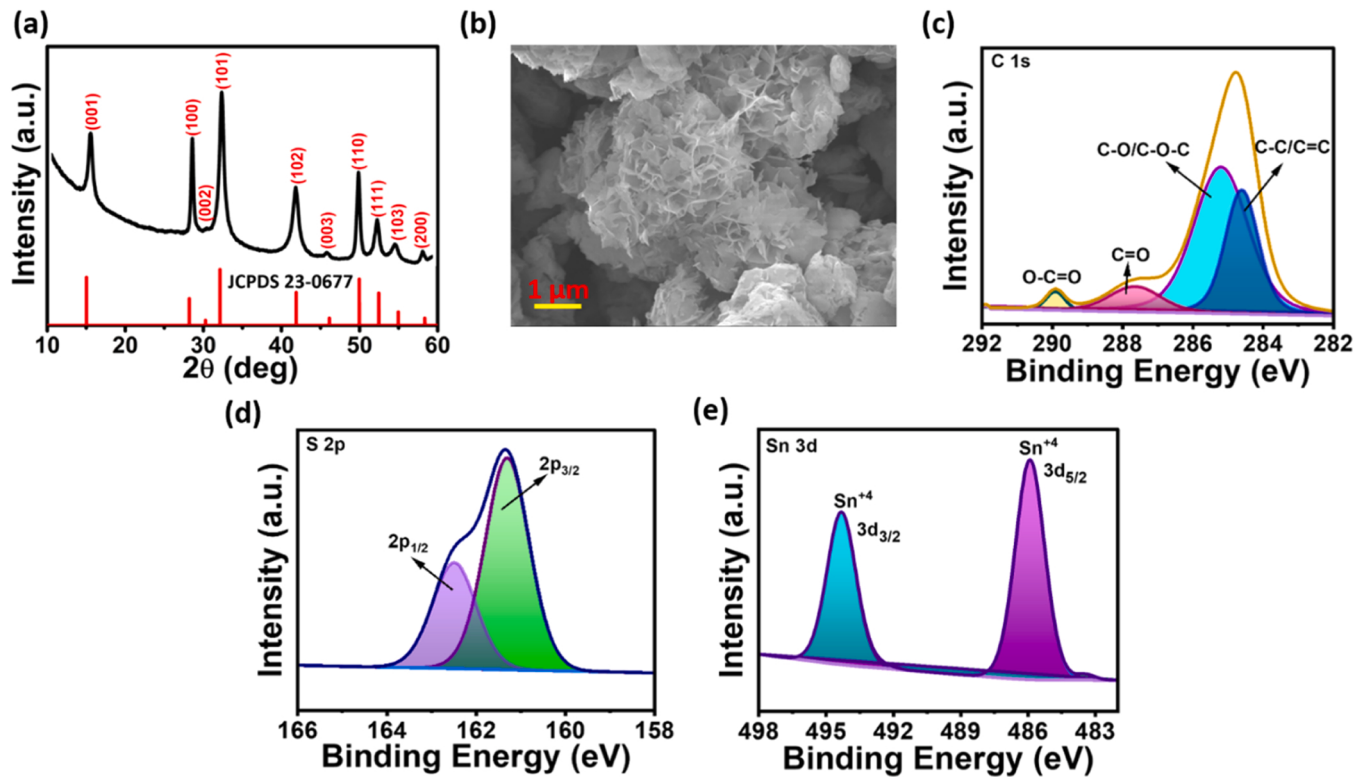


**Fig. 1.** (a) XRD pattern of  $\text{SnS}_2$  nanostructures with JCPDS 23–0677 (b) FESEM photograph of  $\text{SnS}_2$  nanostructures, High-resolution spectra of (c) C 1 s, (d) S 2p, (e) Sn 3d elements from  $\text{SnS}_2$  nanostructures.

resistance varies in response to different gas concentrations. The response of the gas sensor can be calculated from the Eq. (1).

$$\text{Response}(\%) = \frac{R_{\text{sa}}}{R_{\text{NH}_3}} \quad (1)$$

Where  $R_{\text{NH}_3}$  is the sensor's resistance in the presence of  $\text{NH}_3$  gas, and  $R_{\text{sa}}$  is the sensor's resistance in the presence of synthetic air.

### 3. Results and discussion

#### 3.1. Structural and morphological characterization of $\text{SnS}_2$

The Analysis of the crystallinity of the  $\text{SnS}_2$  nanostructures was conducted through XRD. The XRD spectrum, shown in Fig. 1. (a), displays sharp and distinct diffraction peaks that align well with those listed in the Joint Committee on Powder Diffraction Standards (JCPDS) card no. 23–0677. The diffraction peaks in the XRD spectrum indicate a high crystallinity in the  $\text{SnS}_2$  nanostructure and were observed at specific 2θ values of 15.08, 28.50, 30.28, 32.26, 42.03, 46.19, 50.22, 52.66, 55.03, and 58.66 degrees, which correspond to the (001), (100), (002),

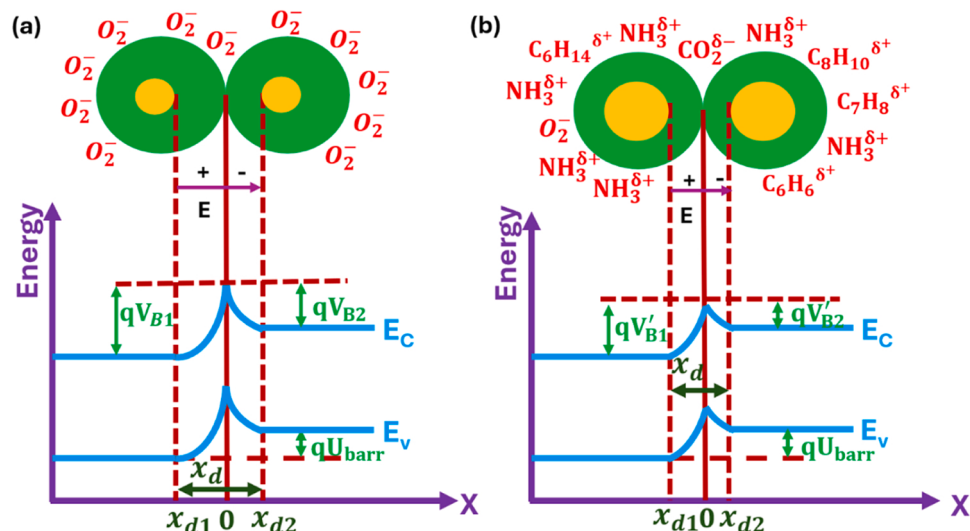


**Fig. 2.** Gas sensing mechanism of  $\text{SnS}_2$  nanostructures with applied voltage in (a) Synthetic air and (b) Target gas environment.

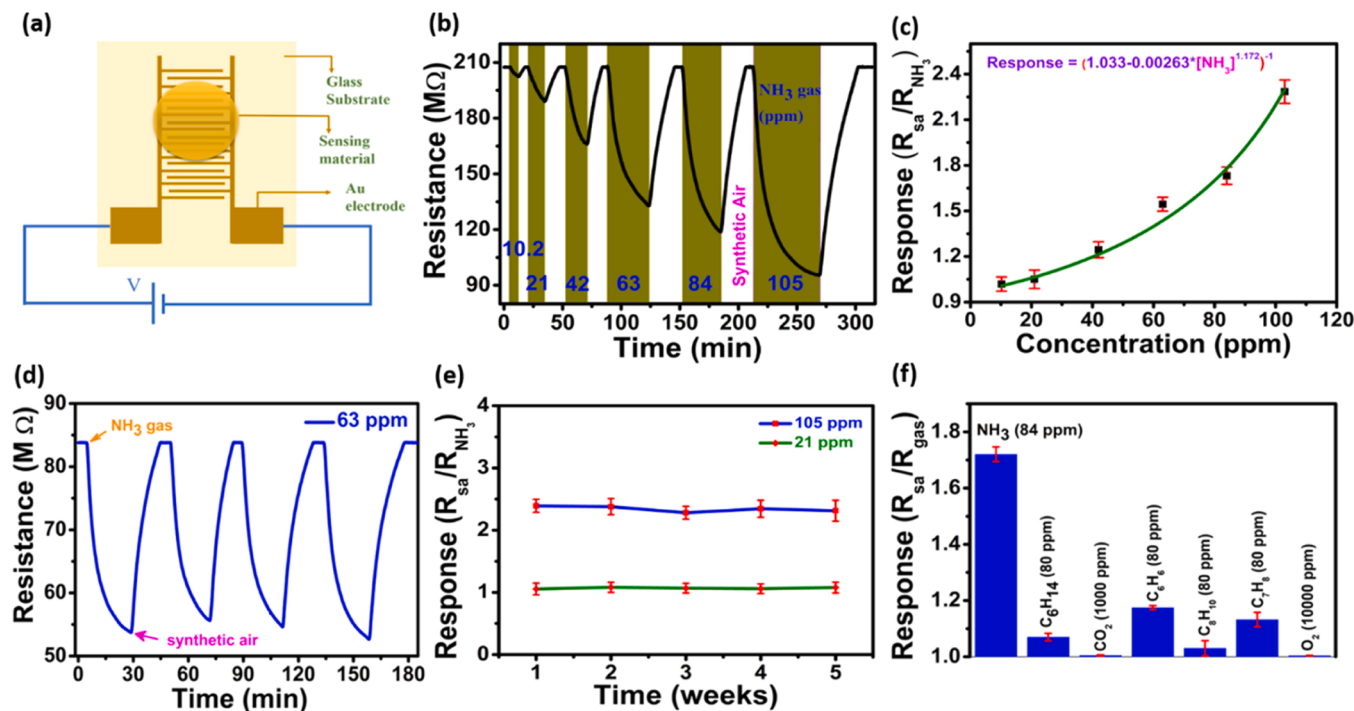


**Fig. 3.** (a) Schematic diagram of the nanostructure-based resistive gas sensor (b) Transient resistance characteristics when exposed to NH<sub>3</sub> gas concentration from 10.2 to 105 ppm (c) Non-linear curve fitting for sensor response vs NH<sub>3</sub> gas concentration regime (10.2–105 ppm) (d) Repeatability of the sensor upon exposure to NH<sub>3</sub> gas at 63 ppm (e) Stability of the sensor upon exposure to NH<sub>3</sub> gas at 63 and 105 ppm (f) Cross-sensitivity to other gases such as C<sub>6</sub>H<sub>14</sub>, CO<sub>2</sub>, C<sub>6</sub>H<sub>6</sub>, C<sub>8</sub>H<sub>10</sub>, C<sub>7</sub>H<sub>8</sub>, and O<sub>2</sub>.

(101), (102), (003), (110), (111), (103), and (200) crystallographic planes, respectively. The peaks observed in the spectrum confirm that the SnS<sub>2</sub> nanostructure possesses a hexagonal crystal structure with lattice constants of  $a = 3.617 \text{ \AA}$  and  $c = 5.856 \text{ \AA}$  [42,43]. The Scherrer equation (Equation S2 in the Supplementary Information) was used to calculate the crystallite size ( $D$ ; 24.62 nm). FESEM analysis revealed that the SnS<sub>2</sub> nanostructures exhibit a microflower morphology with nano-petal-like features, as depicted in Fig. 1. (b). The surface electronic states and chemical composition of the synthesized SnS<sub>2</sub> nanostructures were thoroughly examined using XPS. XPS offers in-depth information regarding the elemental makeup and the chemical and electronic states of the elements present in the material. The survey spectrum shown in Fig. S4, in the Supplementary Information confirms the existence of tin (Sn), sulfur (S), carbon (C), and oxygen (O) elements on the surface of the SnS<sub>2</sub> nanostructures [44]. XPS analysis examined the binding energies and chemical states of the C 1 s, Sn 3d, and S 2p core levels. Peak fitting was executed using Casa XPS software, with background determination facilitated by the Shirley algorithm. C 1 s was internally charge-corrected to 284.8 eV to ensure precise analysis, as shown in Fig. 1. (c) [45]. In the sulfur (S 2p) region, distinct spin-orbit components were observed, with a 1.18 eV energy separation ( $\Delta S_{2p}$ ) between the S 2p<sub>1/2</sub> and S 2p<sub>3/2</sub> peaks. The S 2p XPS spectrum revealed two prominent peaks at 161.3 eV and 162.5 eV binding energies, corresponding to S 2p<sub>3/2</sub> and S 2p<sub>1/2</sub>, respectively, as depicted in Fig. 1. (d) [46]. The deconvoluted Sn 3d XPS spectra revealed two distinct peaks at approximately 485.9 eV and 494.3 eV, corresponding to the Sn<sup>4+</sup> 3d<sub>5/2</sub> and Sn<sup>4+</sup> 3d<sub>3/2</sub> binding energies, respectively, with a spin-orbit splitting of 8.41 eV, as shown in Fig. 1. (e) [47,48]. Furthermore, the C 1 s spectrum was deconvoluted into four distinct peaks at binding energies of 284.5, 285.2, 287.6, and 289.9 eV, representing C–C/C=C, C–O/C–O–C, C=O, and O=C=O bonds, respectively. The higher binding energies in the carbon spectra suggest the presence of oxidized carbon species, indicating potential surface contamination on the SnS<sub>2</sub> nanostructures. For the SnS<sub>2</sub> nanostructures, the calculated stoichiometry is

SnS<sub>1.84</sub> with a sulfur vacancies defect concentration of ~8 % [49]. Sulfur vacancies in SnS<sub>2</sub> nanostructures enhance gas sensing by increasing active sites, modifying electronic properties, and reducing activation energy for gas interactions [50,51]. With an 8 % sulfur vacancy concentration, SnS<sub>2</sub> becomes highly sensitive, making it an excellent material for resistive gas sensors.

### 3.2. Sensor operating principle

The gas-sensing process intricately involves interactions among the sensing material, the target gas, and surrounding environments, as elucidated through the adsorption-desorption process shown in Fig. 2. Upon exposure to synthetic air, oxygen molecules O<sub>2</sub> are physisorbed onto the surface of the SnS<sub>2</sub> nanostructures, forming adsorbed oxygen molecules O<sub>2(ads)</sub> on the SnS<sub>2</sub> nanostructures surface, as outlined in Eq. (2). These oxygen molecules immobilize the electrons from the SnS<sub>2</sub> nanostructure's conduction band upon adsorption, creating negatively charged adsorbed oxygen ions at room temperature, as outlined in Eq. (3) [52]. This electron capture reduces the electron concentration in SnS<sub>2</sub>, thereby increasing the space charge layer width (x<sub>d</sub>) and increasing the sensor's resistance, as depicted in Fig. 2. (a) [53].



When reducing gas such as NH<sub>3</sub> is introduced, it reacts with the pre-adsorbed O<sub>2(ads)</sub><sup>-</sup> ions. This reaction releases the electrons previously trapped by the oxygen ions, allowing them to return to the SnS<sub>2</sub> nanostructure's conduction band [54]. As a result, the electron density in SnS<sub>2</sub> nanostructures increases, reducing the sensor's resistance and a subsequent increase in current, as illustrated in Fig. 2. (b) [55].

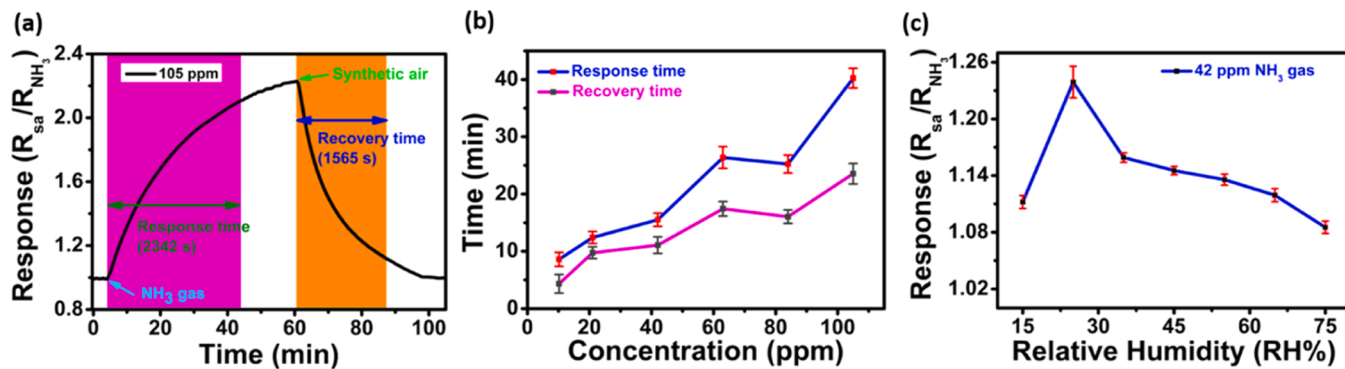


**Fig. 4.** (a) Response and recovery time for NH<sub>3</sub> gas concentration of 105 ppm. (b) Response and recovery times for NH<sub>3</sub> gas concentrations range from 105 to 10.2 ppm (c) Response of the sensor as a function of relative humidity.

### 3.3. Gas sensing performance

The schematic diagram of the SnS<sub>2</sub> nanostructure-based resistive gas sensor is illustrated in Fig. 3. (a). The sensor's response is evaluated by recording current values under a 5 V applied voltage during exposure to NH<sub>3</sub> gas. The transient resistance characteristics under different NH<sub>3</sub> gas concentrations after smoothing with a multiplierless exponential moving average filter (Fig. S5. in the Supplementary Information) are shown in Fig. 3. (b), where a robust 130 % response is observed at 105 ppm NH<sub>3</sub> gas. The heightened response is associated with the unique thin layers of nanostructures, arranged like flowers of SnS<sub>2</sub> nanostructures, which enhance the number of carrier charge transfers and adsorption/desorption reactions. In Fig. 3. (c), the calibration graph illustrates the sensor's steady-state response to NH<sub>3</sub> gas concentration, revealing nonlinearity to the concentration of NH<sub>3</sub> gas, as described in Eq. (4).

$$\text{Response} = \frac{1}{(a + b * x^c)} \quad (4)$$

where constants a (1.033), b (-0.00263), and c (1.172) represent the parameters and x denotes the NH<sub>3</sub> gas concentration. The sensor's repeatability was evaluated by exposing it to 63 ppm NH<sub>3</sub> gas over four consecutive cycles, showing consistent detection with an average response of 1.538 and a low standard deviation of 0.023, as shown in Fig. 3. (d), indicating high repeatability. Although the drop-casting method may not ensure uniform material deposition, the non-compact film allows gas to permeate uniformly, minimizing variations in sensing response. To evaluate the gas sensor's consistent performance, five devices were precisely fabricated under identical conditions and tested at the same gas concentration. The results demonstrated highly

reproducible responses with minimal deviation, as illustrated in Fig. S6. in the Supporting Information. To further evaluate the sensor's stability, it was subjected to periodic testing over five weeks. During this time, the sensor was purged with two different NH<sub>3</sub> gas concentrations, 105 ppm, and 21 ppm, once each week. Fig. 3. (e) demonstrates that the sensor maintained a stable response over five weeks, indicating excellent stability. The sensor's selectivity was also evaluated by the exposure of various other gases, including hexane (C<sub>6</sub>H<sub>14</sub>) at 80 ppm, carbon dioxide (CO<sub>2</sub>) at 1000 ppm, benzene (C<sub>6</sub>H<sub>6</sub>) at 80 ppm, xylene (C<sub>8</sub>H<sub>10</sub>) at 80 ppm, toluene (C<sub>7</sub>H<sub>8</sub>) at 80 ppm and O<sub>2</sub> at 10000 ppm. The response for the NH<sub>3</sub> gas at 84 ppm was compared with its response to other gases. Fig. 3. (f) shows that the sensor responds significantly more to NH<sub>3</sub> gas, confirming its strong selectivity for NH<sub>3</sub> gas detection. The sensor's selectivity to NH<sub>3</sub> can be attributed to the strong dipole moment of NH<sub>3</sub> gas. NH<sub>3</sub> is a polar gas with a high dipole moment of 1.47 D [56]. As a result, NH<sub>3</sub> gas exhibits stronger interactions with the sensing material than non-polar (0 D) or weakly polar gases. The dipole moments of all the tested gases are shown in Table S1 in the Supporting Information. Consequently, NH<sub>3</sub> gas produces a stronger response than other gases. Further, the limit of detection (LOD) and limit of quantification (LOQ) are theoretically determined to be 2 ppm and 4.5 ppm, respectively [57,58].

In gas-sensing applications, response time ( $t_{\text{res}}$ ) and recovery time ( $t_{\text{rec}}$ ) are essential parameters that significantly influence sensor performance. These times denote the interval during which the sensor transitions between the specific percentage of its steady-state value during gas adsorption and desorption processes. For instance, the response time defines the duration required to transition from 0 % to 90 % of its steady-state value during gas adsorption. Conversely, the recovery time denotes the interval to transition from 100 % back to

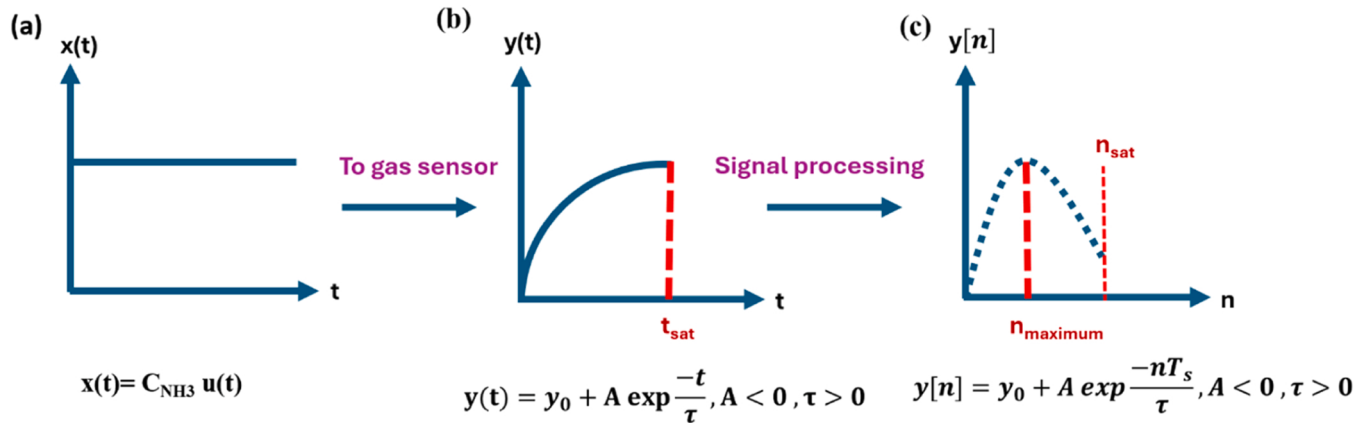


**Fig. 5.** Schematic diagram of transforming the monotonic response to non-monotonic response. (a) target gas concentration (b) Sensor's transient response (c) modified sensor's response with maximum.

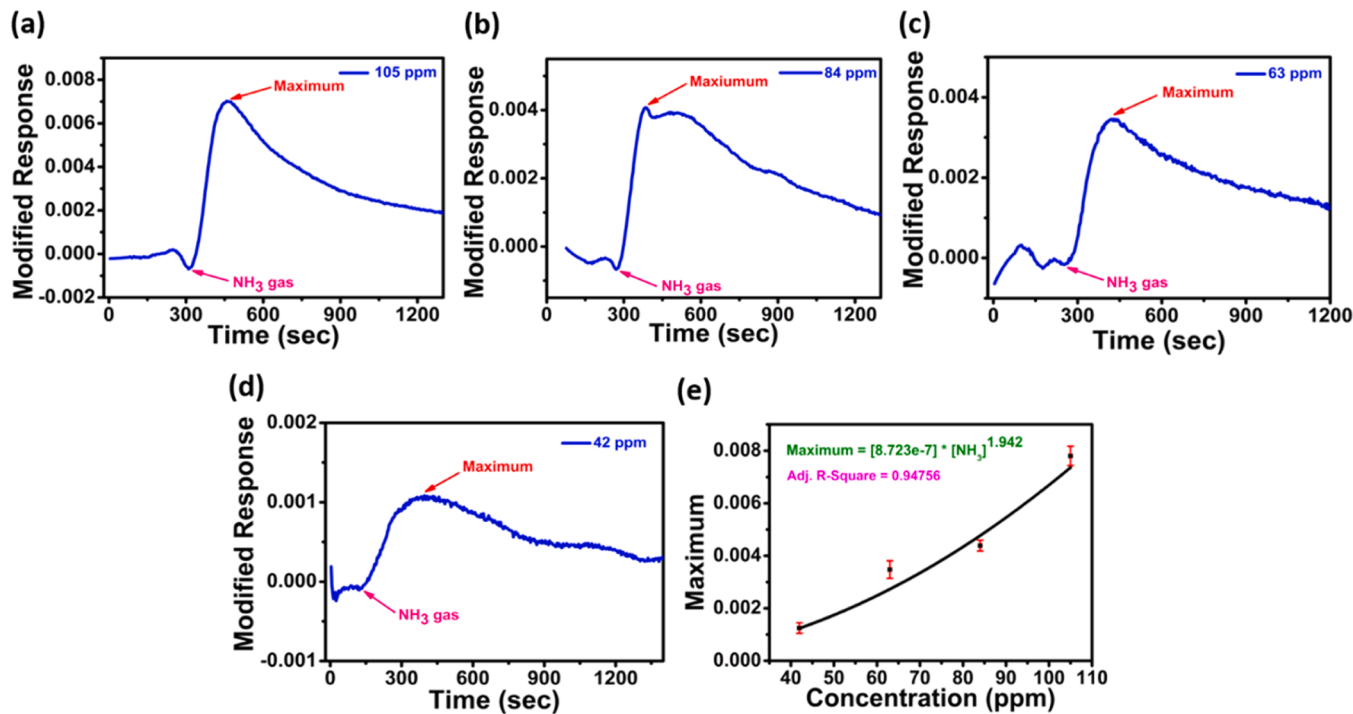


**Fig. 6.** Sensor's maximum response at (a) 105 ppm (b) 84 ppm (c) 63 ppm (d) 42 ppm and (e) Calibration of maximum with NH<sub>3</sub> gas concentration ranging from 42 to 105 ppm.

10 % of its steady-state value during gas desorption. Analyzing dynamic response and recovery characteristics is essential for determining these critical times. Typically, this analysis is graphically represented, as depicted in Fig. 4. (a). Subsequently, calculated response and recovery times for different concentrations of NH<sub>3</sub> gas are illustrated in Fig. 4. (b).

In addition to NH<sub>3</sub> gas, H<sub>2</sub>O is also a highly polar molecule, with dipole moments of 1.85 D and NH<sub>3</sub> is highly soluble in H<sub>2</sub>O [56]. As expected, the sensor is also highly sensitive to humidity in addition to NH<sub>3</sub> gas. To address this issue, the impact of humidity on the gas sensor's response was systematically studied by performing sensing experiments under varying RH levels. The desired RH in the gas sensing chamber was achieved by directing a portion of the synthetic air through a water-filled bubbler controlled by an MFC. Fig. 4. (c) illustrates the sensor's response at room temperature when exposed to 42 ppm NH<sub>3</sub> gas across different RH levels. The sensor's response enhanced as RH increased from 15 % to 25 %, attributed to the adsorption of a limited number of water molecules onto the sensor's surface. These molecules introduced additional active sites, facilitating NH<sub>3</sub> gas adsorption and improving the sensor's performance [59]. Conversely, as RH increased further from 25 % to 75 %, the response declined due to the formation of a thick water layer on the sensor surface. This water layer impeded the availability of active sites and restricted the interaction between NH<sub>3</sub> gas molecules and the sensing material, thereby diminishing the sensor's effectiveness [60–62].

The sensor, however, displays a prolonged response time of around 1000 seconds, which limits its suitability for applications requiring rapid detection. To mitigate this drawback, a specialized signal processing method was developed to shorten the sensor's stabilized response measurement time upon exposure to NH<sub>3</sub> gas, as presented in Fig. 5. Fig. 5. (a) represents the step function, which is the gas concentration. In contrast, the corresponding sensor response follows an exponentially increasing function, as illustrated in Fig. 5. (b). Applying a first-order derivative to the discrete sensor response transforms the output into a nonmonotonic signal with a local peak, as depicted in Fig. 5. (c). Calibrating these maximums against the concentration reduces the maximum response measurement time compared to the

**Table I**  
Comparison of stabilized and maximum response measurement times.

Concentration (ppm)	Stabilized response measurement time (sec)	Maximum response measurement time (sec)	Improvement (%)
105	2342	144	93.85
84	1510	111	92.64
63	1290	104	91.93
42	1303	195	85.03

original steady-state response time ( $n_{\text{sat}}$ ).

Mathematically, the transient response, denoted as  $y(t)$ , of the gas sensor over time  $t$  can be represented with Eq. (5)

$$y(t) = y_0 + A e^{-\frac{t}{\tau}}, \quad A < 0, \quad \tau > 0 \quad (5)$$

The continuous-time exponential function described above is transformed into a discrete-time signal by setting  $t = nT_s$ , where  $T_s$  represents the sampling period. This representation can be expressed in the discrete-time domain with a sampling period of  $T_s$ , as shown in Eq. (6).

$$y[n] = y_0 + A e^{-\frac{nT_s}{\tau}}, \quad A < 0, \quad \tau > 0 \quad (6)$$

The above equation is transformed into a non-monotonic response using a difference equation presented in Eq. (7).

$$y'[n] = y[n] - y[n - 1] \quad (7)$$

The transformed responses corresponding to various concentrations are plotted in Fig. 6. (a) through Fig. 6. (d), while the corresponding maximum values for these concentrations are depicted in Fig. 6. (e). Remarkably, as listed in Table I, the duration to achieve the maximum value is significantly shorter than the time required to stabilize at its steady state. For example, with a 105 ppm NH<sub>3</sub> gas concentration, reaching the maximum value is only 144 seconds, whereas it takes 2342 seconds to achieve a steady-state response. Consequently, utilizing

**Table II**

Comparison of different methods for reducing measurement time.

Method	Improvement in stabilized response measurement time (%)	Resources Requirement	Power consumption	Suitability for low-power applications	Reference
Curve fitting	45	High	High	High	[22]
Exponential moving average	> 80	Low	Moderate	Moderate	[23,29]
Cantor Pairing	Constant (30 sec)	Moderate	Moderate	Moderate	[25]
Neural networks	Not mentioned	Very High	Very High	Very Low	[26–28]
Time normalized response	Not mentioned	Moderate	Moderate	Moderate	[30]
First order differentiation	Upto 94 %	Very low	Very Low	Very High	This work

the maximum value rather than waiting for the steady state can markedly reduce measurement time. Furthermore, the peak value in the modified response is calibrated to the target gas concentration using power law, as explained in Eq. (8).

$$\text{Maximum} = [8.723e - 7] * [\text{NH}_3]^{1.942} \quad (8)$$

Further, to generalize the computational method, the same approach was applied to a polyaniline-based resistive sensor exposed to 2 ppm NH<sub>3</sub> gas. Initially, the sensor exhibited a response time of 531 seconds as shown in Fig. S7. in the [Supplementary Information](#). However, with the implementation of the proposed method, the maximum response measurement time was reduced to 18 seconds, representing a 96 % improvement in measurement time. These findings highlight the effectiveness of the method in enhancing gas sensor performance. Moreover, these results demonstrate that the approach is independent of the sensing material, indicating its potential applicability to a wide range of sensors.

The efficiency of the proposed method is compared with other time reduction techniques in Table II, focusing on stabilized response measurement time reduction, resource requirements, and power consumption. Neural network methods and iterative curve fitting demand substantial resources, making them unsuitable for low-power microcontroller-based applications. While the pairing method, time normalization, and exponential moving average methods are less resource-intensive than neural networks, they still rely on floating point multiplications, consuming significant resources. In contrast, the proposed algorithm is multiplierless, requires minimal resources, and consumes low power. Additionally, it improves maximum response measurement time by up to 94 %, which is noteworthy given the minimal resource requirement. Therefore, the proposed method is highly advantageous for low-cost, low-power applications with resource constraints.

While the proposed multiplierless differentiation technique effectively transforms the monotonically increasing sensor response into a nonmonotonic response with maximum, certain restrictions must be acknowledged: **1. Loss of Low-Frequency Trends** – The differentiation process suppresses slow variations in the sensor response, potentially removing useful long-term drift information. To address this, future work will focus on integrating hybrid approaches that combine differentiation with baseline correction techniques to retain relevant low-frequency components. **2. Dependency on Sampling Rate** – The sensor's sampling rate influences the effectiveness of the proposed approach. Insufficient sampling may lead to missed variations, whereas excessively high sampling rates can introduce unnecessary fluctuations. Future studies will implement an adaptive sampling mechanism to optimize this trade-off and enhance signal fidelity. **3. Sensor Aging Effects** – Long-term variations due to sensor aging can impact the consistency of maximum detection. To mitigate this, future research will incorporate self-calibration mechanisms to improve long-term stability and robustness. **4. Validity in the Presence of Cross-Interference** – Real-world sensing environments involve multiple gases, leading to cross-interference that may introduce spurious peaks or affect maximum detection. Future work will evaluate the approach under multi-gas conditions and develop compensation strategies to improve selectivity

and reliability. Alternatively, dielectric passivation will be used, as it can introduce fixed charges that influence the adsorption of gas molecules on the semiconductor surface. Since this study applies to both positively and negatively adsorbed ions, which cause variations in sensor resistance in different directions, passivation can enhance sensitivity and selectivity in detecting various gases. [63,64].

#### 4. Conclusion

In summary, a novel strategy has been introduced to mitigate the challenge of slow response times in gas sensors operating at room temperature. This method was demonstrated using a resistive sensor fabricated with SnS<sub>2</sub> nanostructures synthesized through a solvothermal process. The sensor was tested with ammonia gas, and the proposed stabilized response measurement time reduction algorithm was applied to optimize its response. The algorithm successfully reduced the maximum response measurement time by up to 94 % compared to conventional methods. This approach effectively tackles the challenge of slow response in gas sensors that exhibit excellent response. Moreover, the technique is versatile and can be applied to any sensor with a monotonically varying response over time, making it a powerful tool for improving the performance of different types of sensors. While the proposed method significantly enhances measurement efficiency for single-gas detection, real-world applications often involve complex gas mixtures where cross-sensitivity can impact sensor performance. Additionally, factors such as the response sampling rate, sensor aging, and drift can impact maximum detection. Therefore, future work will focus on integrating baseline correction to retain low-frequency trends, implementing adaptive sampling to optimize signal fidelity, incorporating self-calibration to address aging effects and enhancing selectivity in multi-gas environments.

#### Author Statement

I, the undersigned, declare that this manuscript is original, has not been published previously, and is not currently under consideration for publication elsewhere. I confirm that all named authors have read and approved the manuscript and that no individuals who meet the authorship criteria have been omitted. Furthermore, I confirm that all contributors have approved the order of authors listed in the manuscript. I understand that the Corresponding Author serves as the primary contact for the editorial process and is responsible for communicating with the other authors regarding progress, submission of revisions, and final approval of proofs.

#### CRediT authorship contribution statement

**BANDARI NAVEEN KUMAR:** Writing – review & editing, Writing – original draft, Methodology, Formal analysis, Conceptualization.  
**KANAPARTHI SRINIVASULU:** Methodology, Conceptualization. **Singh**

**Shiv Govind:** Writing – review & editing, Supervision.

## Declaration of Competing Interest

The authors declare that they have no known competing financial interests or personal relationships that could have appeared to influence the work reported in this paper.

## Acknowledgment

The authors thank the Department of Electrical Engineering at the Indian Institute of Technology Hyderabad for their invaluable support. This research was funded under the Quality Improvement Program (QIP) of the All-India Council for Technical Education (AICTE), which provided essential assistance in facilitating the project.

## Appendix A. Supporting information

Supplementary data associated with this article can be found in the online version at [doi:10.1016/j.sna.2025.116442](https://doi.org/10.1016/j.sna.2025.116442).

## Data availability

Data will be made available on request.

## References

- [1] T.A. Saleh, G. Fadillah, Green synthesis protocols, toxicity, and recent progress in nanomaterial-based for environmental chemical sensors applications, *Trends Environ. Anal. Chem.* 39 (2023) e00204, <https://doi.org/10.1016/j.teac.2023.e00204>.
- [2] D.M.G. Preethichandra, M.D. Gholami, E.L. Izake, A.P. O'Mullane, P. Sonar, Conducting Polymer Based Ammonia and Hydrogen Sulfide Chemical Sensors and Their Suitability for Detecting Food Spoilage, *Adv. Mater. Technol.* 8 (2023) 2200841, <https://doi.org/10.1002/admt.202200841>.
- [3] R.J. Rath, S. Farajikhah, F. Oveissi, F. Dehghani, S. Naficy, Chemiresistive Sensor Arrays for Gas/Volatile Organic Compounds Monitoring: A Review, *Adv. Eng. Mater.* 25 (2023) 2200830, <https://doi.org/10.1002/adem.202200830>.
- [4] X. Chen, C. Yao, Z. Li, Microarray-based chemical sensors and biosensors: Fundamentals and food safety applications, *TrAC Trends Anal. Chem.* 158 (2023) 116785, <https://doi.org/10.1016/j.trac.2022.116785>.
- [5] K. Khan, A.K. Tareen, M. Iqbal, Z. Ye, Z. Xie, A. Mahmood, N. Mahmood, H. Zhang, Recent Progress in Emerging Novel MXenes Based Materials and their Fascinating Sensing Applications, *Small* 19 (2023) 2206147, <https://doi.org/10.1002/smll.202206147>.
- [6] S. Kanaparthi, S.G. Singh, MoS<sub>2</sub> Chemiresistive Sensor Array on Paper Patterned with Toner Lithography for Simultaneous Detection of NH<sub>3</sub> and H<sub>2</sub>S Gases, *ACS Sustain. Chem. Eng.* 9 (2021) 14735–14743, <https://doi.org/10.1021/acscuschemeng.1c04166>.
- [7] Z. Zhang, X. Liu, H. Zhou, S. Xu, C. Lee, Advances in Machine-Learning Enhanced Nanosensors: From Cloud Artificial Intelligence Toward Future Edge Computing at Chip Level, *Small Struct.* 5 (2024) 2300325, <https://doi.org/10.1002/sstr.202300325>.
- [8] S. Kanaparthi, S.G. Singh, Discrimination of gases with a single chemiresistive multi-gas sensor using temperature sweeping and machine learning, *Sens. Actuators B: Chem.* 348 (2021) 130725, <https://doi.org/10.1016/j.snb.2021.130725>.
- [9] B. Tsizh, O. Aksimentyeva, Ways to improve the parameters of optical gas sensors of ammonia based on polyaniline, *Sens. Actuators A: Phys.* 315 (2020) 112273, <https://doi.org/10.1016/j.sna.2020.112273>.
- [10] T. Addabbo, A. Fort, M. Mugnaini, V. Vignoli, A. Baldi, M. Bruzzi, Quartz-Crystal Microbalance Gas Sensors Based on TiO<sub>2</sub> Nanoparticles, *IEEE Trans. Instrum. Meas.* 67 (2018) 722–730, <https://doi.org/10.1109/TIM.2017.2785118>.
- [11] M. Serafini, F. Mariani, I. Gualandi, F. Decataldo, L. Possanzini, M. Tessarolo, B. Fraboni, D. Tonelli, E. Scavetta, A Wearable Electrochemical Gas Sensor for Ammonia Detection, *Sensors* 21 (2021) 7905, <https://doi.org/10.3390/s21237905>.
- [12] A. Roy, A. Ray, P. Sadhukhan, K. Naskar, G. Lal, R. Bhar, C. Sinha, S. Das, Polyaniline-multiwalled carbon nanotube (PANI-MWCNT): Room temperature resistive carbon monoxide (CO) sensor, *Synth. Met.* 245 (2018) 182–189, <https://doi.org/10.1016/j.synthmet.2018.08.024>.
- [13] M. Li, X. Gao, Y. Zhang, Y. Zheng, Z. Lin, G. Wei, Ammonia Sensing Properties of SnS<sub>2</sub>/SnO<sub>2</sub> Nanocomposite-Based Gas Sensor by SnS<sub>2</sub> Annealing, *IEEE Sens. J.* 22 (2022) 23456–23463, <https://doi.org/10.1109/JSEN.2022.3215156>.
- [14] Biosensors for Food Spoilage Detection: A Comprehensive Review of Current Advances, *J. Food Chem. Nanotechnol.* 10 (2024), <https://doi.org/10.17756/jfcn.2024-s1-010>.
- [15] M.O. Oduoye, Z. Olaide, A.A. Adegoke, M.T. Agbaje, A. Akilimali, M. Lawal, The Roles of Redox and Enzymatic Processes in Food Spoilage in the Global South, in: M.C. Ogwu, S.C. Izah, N.R. Ntuli (Eds.), *Food Safety and Quality in the Global South*, Springer Nature Singapore, Singapore, 2024, pp. 601–624, [https://doi.org/10.1007/978-981-97-2428-4\\_19](https://doi.org/10.1007/978-981-97-2428-4_19).
- [16] S. Matindoust, A. Farzi, M. Baghaei Nejad, M.H. Shahrokh Abadi, Z. Zou, L.-R. Zheng, Ammonia gas sensor based on flexible polyaniline films for rapid detection of spoilage in protein-rich foods, *J. Mater. Sci: Mater. Electron.* 28 (2017) 7760–7768, <https://doi.org/10.1007/s10854-017-6471-z>.
- [17] L. Van Duy, T.T. Nguyet, D.T.T. Le, N. Van Duy, H. Nguyen, F. Biasioli, M. Tonezzer, C. Di Natale, N.D. Hoa, Room Temperature Ammonia Gas Sensor Based on p-Type-like V<sub>2</sub>O<sub>5</sub> Nanosheets towards Food Spoilage Monitoring, *Nanomaterials* 13 (2022) 146, <https://doi.org/10.3390/nano13010146>.
- [18] S. Robbiani, B.J. Lotesoriere, R.L. Dellacà, L. Capelli, Physical Confounding Factors Affecting Gas Sensors Response: A Review on Effects and Compensation Strategies for Electronic Nose Applications, *Chemosensors* 11 (2023) 514, <https://doi.org/10.3390/chemosensors11100514>.
- [19] M. Shooshtari, A. Salehi, S. Vollebregt, Effect of Humidity on Gas Sensing Performance of Carbon Nanotube Gas Sensors Operated at Room Temperature, *IEEE Sens. J.* 21 (2021) 5763–5770, <https://doi.org/10.1109/JSEN.2020.3038647>.
- [20] X. Pan, X. Zhao, J. Chen, A. Bermak, Z. Fan, A fast-response/recovery ZnO hierarchical nanostructure based gas sensor with ultra-high room-temperature output response, *Sens. Actuators B: Chem.* 206 (2015) 764–771, <https://doi.org/10.1016/j.snb.2014.08.089>.
- [21] L. Zhihua, Z. Xucheng, S. Jiyoung, Z. Xiaobo, H. Xiaowei, H.E. Tahir, M. Holmes, Fast response ammonia sensor based on porous thin film of polyaniline/sulfonated nickel phthalocyanine composites, *Sens. Actuators B: Chem.* 226 (2016) 553–562, <https://doi.org/10.1016/j.snb.2015.10.062>.
- [22] D.L. Osorio-Arrieta, J.L. Muñoz-Mata, G. Beltrán-Pérez, J. Castillo-Mixcoatl, C. O. Mendoza-Barrera, V. Altuzar-Aguilar, S. Muñoz-Aguirre, Reduction of the Measurement Time by the Prediction of the Steady-State Response for Quartz Crystal Microbalance Gas Sensors, *Sensors* 18 (2018) 2475, <https://doi.org/10.3390/s18082475>.
- [23] J. Burgues, S. Marco, Wind-Independent Estimation of Gas Source Distance From Transient Features of Metal Oxide Sensor Signals, *IEEE Access* 7 (2019) 140460–140469, <https://doi.org/10.1109/ACCESS.2019.2940936>.
- [24] O. Casas, F.I. Rillo, Method for reducing response time in sensor measurement, *Rev. Sci. Instrum.* 80 (2009) 085102, <https://doi.org/10.1063/1.3193717>.
- [25] S. Kanaparthi, S.G. Singh, Reduction of the Measurement Time of a Chemiresistive Gas Sensor Using Transient Analysis and the Cantor Pairing Function, *ACS Meas. Sci. Au* 2 (2022) 113–119, <https://doi.org/10.1021/acsmeasuresci.1c00043>.
- [26] Q. Zhang, S. Li, W. Tang, X. Guo, Fast Measurement With Chemical Sensors Based on Sliding Window Sampling and Mixed-Feature Extraction, *IEEE Sens. J.* 20 (2020) 8740–8745, <https://doi.org/10.1109/JSEN.2020.2985034>.
- [27] J. Culic Gambiroza, T. Mastelic, T. Kovacevic, M. Cagalj, Predicting Low-Cost Gas Sensor Readings From Transients Using Long Short-Term Memory Neural Networks, *IEEE Internet Things J.* 7 (2020) 8451–8461, <https://doi.org/10.1109/JIOT.2020.2990526>.
- [28] J. Fonollosa, S. Sheik, R. Huerta, S. Marco, Reservoir computing compensates slow response of chemosensor arrays exposed to fast varying gas concentrations in continuous monitoring, *Sens. Actuators B: Chem.* 215 (2015) 618–629, <https://doi.org/10.1016/j.snb.2015.03.028>.
- [29] M.K. Muezzinoglu, A. Vergara, R. Huerta, N. Rulkov, M.I. Rabinovich, A. Selverston, H.D.I. Abarbanel, Acceleration of chemo-sensory information processing using transient features, *Sens. Actuators B: Chem.* 137 (2009) 507–512, <https://doi.org/10.1016/j.snb.2008.10.065>.
- [30] E. Castillo, J.F. Salmeron, A. Falco, F.C. Loghin, F.J. Romero, P. Lugli, D. P. Morales, A. Rivadeneira, An Optimized Measurement Algorithm for Gas Sensors Based on Carbon Nanotubes: Optimizing Sensor Performance and Hardware Resources, *IEEE Internet Things J.* 6 (2019) 9140–9146, <https://doi.org/10.1109/JIOT.2019.298231>.
- [31] J.L. Munoz-Mata, D.L. Osorio-Arrieta, J.J. Jimenez-Arellano, G. Beltran-Perez, J. Castillo-Mixcoatl, S. Munoz-Aguirre, Comparison of Two Methods to Reduce Time Measurement of Quartz Crystal Microbalance Gas Sensors, in: 2019 IEEE International Symposium on Olfaction and Electronic Nose (ISOEN), IEEE, Fukuoka, Japan, 2019, pp. 1–4, <https://doi.org/10.1109/ISOEN.2019.8823192>.
- [32] M. Luo, D. Xiong, X. Huang, S. Cai, S. Li, Z. Jia, Z. Gao, V<sub>2</sub>CTx@PANI nanocomposite as a highly effective room temperature gas sensor for ammonia detection, *J. Alloy. Compd.* 1006 (2024) 176340, <https://doi.org/10.1016/j.jallcom.2024.176340>.
- [33] S. Kanaparthi, S. Govind Singh, Highly sensitive and ultra-fast responsive ammonia gas sensor based on 2D ZnO nanoflakes, *Mater. Sci. Energy Technol.* 3 (2020) 91–96, <https://doi.org/10.1016/j.mset.2019.10.010>.
- [34] C. Mackin, V. Schröder, A. Zurutza, C. Su, J. Kong, T.M. Swager, T. Palacios, Chemiresistive Graphene Sensors for Ammonia Detection, *ACS Appl. Mater. Interfaces* 10 (2018) 16169–16176, <https://doi.org/10.1021/acsami.8b00853>.
- [35] P. Vashishtha, A. Dash, S. Walia, G. Gupta, Self-bias Mo–Sb–Ga multilayer photodetector encompassing ultra-broad spectral response from UV–C to IR–B, *Opt. Laser Technol.* 181 (2025) 111705, <https://doi.org/10.1016/j.optlastec.2024.111705>.
- [36] P. Vashishtha, P. Prajapat, K. Kumar, M. Kumar, S. Walia, G. Gupta, Multiband spectral response inspired by ultra-high responsive thermally stable and self-powered Sb<sub>2</sub>Se<sub>3</sub>/GaN heterojunction based photodetector, *Surf. Interfaces* 42 (2023) 103376, <https://doi.org/10.1016/j.surfin.2023.103376>.

- [37] P. Vashishtha, R. Tanwar, S. Gautam, L. Goswami, S.S. Kushwaha, G. Gupta, Wavelength-modulated polarity switch self-powered Bi<sub>2</sub>Se<sub>3</sub>/GaN heterostructure photodetector, Mater. Sci. Semicond. Process. 180 (2024) 108553, <https://doi.org/10.1016/j.mssp.2024.108553>.
- [38] P. Vashishtha, A. Dash, P. Prajapat, P. Goswami, S. Walia, G. Gupta, Self-Powered Broadband Photodetection of MoS<sub>2</sub> /Sb<sub>2</sub> Se<sub>3</sub> Heterostructure, ACS Appl. Opt. Mater. 1 (2023) 1952–1962, <https://doi.org/10.1021/acsaom.3c00300>.
- [39] P. Vashishtha, P. Goswami, P. Prajapat, A. Kumar Gangwar, P. Singh, G. Gupta, Highly efficient, self-powered, and air-stable broadband photodetector based on SnSe thin film, Mater. Sci. Eng.: B 297 (2023) 116808, <https://doi.org/10.1016/j.mseb.2023.116808>.
- [40] J. Wuloh, E.S. Agorka, N.O. Boadi, Modification of Metal Oxide Semiconductor Gas Sensors Using Conducting Polymer Materials, J. Sens. 2023 (2023) 7427986, <https://doi.org/10.1155/2023/7427986>.
- [41] Y. Jiang, L. Wu, Q. Chen, N. Li, J. Tian, High-performance capacitive humidity sensor based on flower-like SnS<sub>2</sub>/Ti<sub>3</sub>C<sub>2</sub> MXene for respiration monitoring and non-contact sensing, Sens. Actuators B: Chem. 426 (2025) 137012, <https://doi.org/10.1016/j.snb.2024.137012>.
- [42] W. Xu, Z. Xie, X. Cui, K. Zhao, L. Zhang, G. Dietrich, K.M. Dooley, Y. Wang, Hierarchical Graphene-Encapsulated Hollow SnO<sub>2</sub>@SnS<sub>2</sub> Nanostructures with Enhanced Lithium Storage Capability, ACS Appl. Mater. Interfaces 7 (2015) 22533–22541, <https://doi.org/10.1021/acsami.5b06765>.
- [43] Y. Xiong, W. Xu, D. Ding, W. Lu, L. Zhu, Z. Zhu, Y. Wang, Q. Xue, Ultra-sensitive NH<sub>3</sub> sensor based on flower-shaped SnS<sub>2</sub> nanostructures with sub-ppm detection ability, J. Hazard. Mater. 341 (2018) 159–167, <https://doi.org/10.1016/j.jhazmat.2017.07.060>.
- [44] Z. Qin, K. Xu, H. Yue, H. Wang, J. Zhang, C. Ouyang, C. Xie, D. Zeng, Enhanced room-temperature NH<sub>3</sub> gas sensing by 2D SnS<sub>2</sub> with sulfur vacancies synthesized by chemical exfoliation, Sens. Actuators B: Chem. 262 (2018) 771–779, <https://doi.org/10.1016/j.snb.2018.02.060>.
- [45] D. Gu, X. Wang, W. Liu, X. Li, S. Lin, J. Wang, M.N. Rumyantseva, A.M. Gaskov, S. A. Akbar, Visible-light activated room temperature NO<sub>2</sub> sensing of SnS<sub>2</sub> nanosheets based chemiresistive sensors, Sens. Actuators B: Chem. 305 (2020) 127455, <https://doi.org/10.1016/j.snb.2019.127455>.
- [46] T. Wang, J. Liu, Y. Zhang, Q. Liang, R. Wu, H.-S. Tsai, Y. Wang, J. Hao, Bifunctional gas sensor based on Bi<sub>2</sub>S<sub>3</sub>/SnS<sub>2</sub> heterostructures with improved selectivity through visible light modulation, J. Mater. Chem. A 10 (2022) 4306–4315, <https://doi.org/10.1039/DITA0461F>.
- [47] Z. Yang, C. Su, S. Wang, Y. Han, X. Chen, S. Xu, Z. Zhou, N. Hu, Y. Su, M. Zeng, Highly sensitive NO<sub>2</sub> gas sensors based on hexagonal SnS<sub>2</sub> nanoplates operating at room temperature, Nanotechnology 31 (2020) 075501, <https://doi.org/10.1088/1361-6528/ab5271>.
- [48] P. Bharathi, S. Harish, M. Shimomura, M.K. Mohan, J. Archana, M. Navaneethan, Ultrasensitive and reversible NO<sub>2</sub> gas sensor based on SnS<sub>2</sub>/TiO<sub>2</sub> heterostructures for room temperature applications, Chemosphere 346 (2024) 140486, <https://doi.org/10.1016/j.chemosphere.2023.140486>.
- [49] P. Vashishtha, I.H. Abidi, S.P. Giridhar, A.K. Verma, P. Prajapat, A. Bhoriya, B. J. Murdoch, J.O. Tollerud, C. Xu, J.A. Davis, G. Gupta, S. Walia, CVD-Grown Monolayer MoS<sub>2</sub> and GaN Thin Film Heterostructure for a Self-Powered and Bidirectional Photodetector with an Extended Active Spectrum, ACS Appl. Mater. Interfaces 16 (2024) 31294–31303, <https://doi.org/10.1021/acsami.4c03902>.
- [50] R. Zhao, T. Wang, M. Zhao, C. Xia, X. Zhao, Y. An, X. Dai, A theoretical simulation of small-molecules sensing on an S-vacancy SnS<sub>2</sub> monolayer, Phys. Chem. Chem. Phys. 19 (16) (2017) 10470–10480.
- [51] R. Li, K. Jiang, S. Chen, Z. Lou, T. Huang, D. Chen, G. Shen, SnO<sub>2</sub>/SnS<sub>2</sub> nanotubes for flexible room-temperature NH<sub>3</sub> gas sensors, RSC Adv. 7 (83) (2017) 52503–52509.
- [52] R.K. Mishra, H.J. Choi, J.W. Ryu, G.J. Choi, V. Kumar, P. Kumar, J. Singh, S. Kumar, J.S. Gwag, Recent progress in gas sensing based on 2D SnS<sub>2</sub> and its heterostructure platforms: A review, Sens. Actuators A: Phys. 365 (2024) 114860, <https://doi.org/10.1016/j.sna.2023.114860>.
- [53] X. Jiang, Y. Zhen, Y. Feng, Z. Yang, Z. Qin, Synthesis of SnS<sub>2</sub>/SnO<sub>2</sub> nano-heterojunctions with increased reactive sites and charge transfer for ultrasensitive NH<sub>3</sub> detection, J. Alloy. Compd. 938 (2023) 168520, <https://doi.org/10.1016/j.jallcom.2022.168520>.
- [54] T. Wang, G. Liu, D. Zhang, D. Wang, F. Chen, J. Guo, Fabrication and properties of room temperature ammonia gas sensor based on SnO<sub>2</sub> modified WSe<sub>2</sub> nanosheets heterojunctions, Appl. Surf. Sci. 597 (2022) 153564, <https://doi.org/10.1016/j.apsusc.2022.153564>.
- [55] B. Zhang, Y. Liu, T. Liang, T. Sakthivel, L. Yu, Z. Dai, Activating the Basal Plane of Defective SnS<sub>2</sub> Nanosheets for NH<sub>3</sub> Gas Sensing, ACS Appl. Nano Mater. 3 (2020) 4642–4653, <https://doi.org/10.1021/acsnano.0c00649>.
- [56] L. Monchick, E.A. Mason, Transport Properties of Polar Gases, J. Chem. Phys. 35 (1961) 1676–1697, <https://doi.org/10.1063/1.1732130>.
- [57] L.A. Currie, Nomenclature in evaluation of analytical methods including detection and quantification capabilities (IUPAC Recommendations 1995), Pure Appl. Chem. 67 (1995) 1699–1723, <https://doi.org/10.1351/pac199567101699>.
- [58] R.K. Jha, J.V. D'Costa, N. Sakhuja, N. Bhat, MoSe<sub>2</sub> nanoflakes based chemiresistive sensors for ppb-level hydrogen sulfide gas detection, Sens. Actuators B: Chem. 297 (2019) 126687, <https://doi.org/10.1016/j.snb.2019.126687>.
- [59] V.R. Naganaboina, S.G. Singh, CdS based chemiresistor with Schottky contact: Toxic gases detection with enhanced sensitivity and selectivity at room temperature, Sens. Actuators B: Chem. 357 (2022) 131421, <https://doi.org/10.1016/j.snb.2022.131421>.
- [60] S.B. Kulkarni, Y.H. Navale, F.J. Stadler, N.S. Ramgir, V.B. Patil, Hybrid polyaniline-WO<sub>3</sub> flexible sensor: A room temperature competence towards NH<sub>3</sub> gas, Sens. Actuators B: Chem. 288 (2019) 279–288, <https://doi.org/10.1016/j.snb.2019.02.094>.
- [61] Y. Zhang, Y. Jiang, Z. Duan, Q. Huang, Y. Wu, B. Liu, Q. Zhao, S. Wang, Z. Yuan, H. Tai, Highly sensitive and selective NO<sub>2</sub> sensor of alkalinized V<sub>2</sub>CT MXene driven by interlayer swelling, Sens. Actuators B: Chem. 344 (2021) 130150, <https://doi.org/10.1016/j.snb.2021.130150>.
- [62] D. Gu, X. Wang, W. Liu, X. Li, S. Lin, J. Wang, M.N. Rumyantseva, A.M. Gaskov, S. A. Akbar, Visible-light activated room temperature NO<sub>2</sub> sensing of SnS<sub>2</sub> nanosheets based chemiresistive sensors, Sens. Actuators B: Chem. 305 (2020) 127455, <https://doi.org/10.1016/j.snb.2019.127455>.
- [63] S. Mamataj, B. Roy, D. Datta, R. Dutta, B. Das, Sensing Performance Analysis of Passivated  $\beta$ -(AlxGa1-x)2 O<sub>3</sub>/Ga<sub>2</sub>O<sub>3</sub> Schottky Diode Gas Sensor with Catalytic Metals at High Temperature, J. Inst. Eng. India Ser. B (2024), <https://doi.org/10.1007/s40031-024-01182-0>.
- [64] T. Sugiura, S. Matsumoto, N. Nakano, Numerical analysis of tunnel oxide passivated contact solar cell performances for dielectric thin film materials and bulk properties, Sol. Energy 214 (2021) 205–213, <https://doi.org/10.1016/j.solener.2020.11.032>.

**Naveen Kumar Bandari** received his B.Tech in Electronics and Communication Engineering from Ramappa Engineering College, Warangal, India, in 2007 and his M.Tech degree in VLSI-System Design from the National Institute of Technology (NIT) Warangal, India, in 2012. He is pursuing his Ph.D. as a Research Scholar in the Department of Electrical Engineering at the Indian Institute of Technology (IIT) Hyderabad, India. His research focuses on chemiresistive gas sensors with environmental monitoring and healthcare applications.

**Srinivasulu Kanaparthi** obtained his B.Tech in Electronics and Communication Engineering from Jawaharlal Nehru Technological University, Kakinada, India, in 2011 and later completed his M.Tech in Microelectronics and VLSI at the Indian Institute of Technology (IIT) Hyderabad, India, in 2016. He is a Research Associate in the Department of Electrical Engineering at the Indian Institute of Technology (IIT) Hyderabad, India. His research interests encompass flexible electronics, environmental monitoring and healthcare sensors, and sensor signal processing.

**Shiv Govind Singh** completed his M.Tech at the Indian Institute of Technology (IIT) Kanpur, India, and earned his Ph.D. from the Indian Institute of Technology (IIT) Bombay, India. Currently, he is a professor in the Department of Electrical Engineering at the Indian Institute of Technology (IIT) Hyderabad, India. His research interests include 3D IC integration, Quantum Computing, micro & nanoelectronics, microfluidics, Biosensors, Gas sensors, Lab on Chip, and MEMS/NEMS.